

Aeroelastic Dynamic Response and Control of an Airfoil Section

with Control Surface Nonlinearities

Daochun Li^{1,2}, Shijun Guo¹, Jinwu Xiang²

¹Aerospace Engineering, Cranfield University, Cranfield, Beds, MK43 0AL, UK

²Beijing University of Aeronautics and Astronautics, Beijing 100083, P.R. China

Abstract Nonlinearities in aircraft mechanisms are inevitable, especially in the control system. It's necessary to investigate the effects of them on the dynamic response and control performance of aeroelastic system. In this paper, based on the state-dependent Riccati equation method, a state feedback suboptimal control law is derived for aeroelastic response and flutter suppression of a three degree-of-freedom typical airfoil section. With the control law designed, nonlinear effects of freeplay in the control surface and time delay between the control input and actuator are investigated by numerical approach. A cubic nonlinearity in pitch degree is adopted to prevent the aeroelastic responses from divergence when the flow velocity exceeds the critical flutter speed. For the system with a freeplay, the responses of both open- and closed-loop systems are determined with Runge-Kutta algorithm in conjunction with Henon's method. This method is used to locate the switching points accurately and efficiently as the system moves from one subdomain into another. The simulation results show that the freeplay leads to a forward phase response and a slight increase of flutter speed of the closed-loop system. The effect of freeplay on the aeroelastic response decreases as the flow velocity increases. The time delay between the control input and actuator may impair control performance and cause high-frequency motion and quasi-periodic vibration.

Keywords: aeroelasticity; freeplay nonlinearity; time delay; limit cycle oscillation; state-dependent Riccati equation

Nomenclature

a	=	non-dimensional distance from airfoil mid-chord to elastic axis
b	=	airfoil semi-chord
$C(k)$	=	generalized Theodorsen function
c	=	non-dimensional distance from airfoil mid-chord to the control surface hinge line
c_i	=	coefficients of Wagner's function
h	=	plunge displacement
J	=	performance index of optimal problem
k	=	reduced frequency
L	=	aerodynamic lift
M_α, M_β	=	aerodynamic moment of wing-aileron and of aileron
m	=	mass of wing-aileron (per unit span)
m_t	=	total mass of wing-aileron and support blocks (per unit span)
\mathbf{Q}	=	state coefficient matrix in performance index
r	=	control input coefficient in performance index
r_α	=	radius of gyration of wing-aileron
r_β	=	reduced radius of gyration of aileron
t	=	time
t_a	=	time when the control is turned on
U	=	free stream velocity
\mathbf{x}_a	=	vector of augmented variables
x_α	=	non-dimensional distance from airfoil elastic axis to center of mass
x_β	=	non-dimensional distance from aileron hinge line to center of mass
α	=	pitch angle about the elastic axis
β	=	aileron displacement about the hinge line
β_c	=	control input

δ	=	freeplay region
γ	=	cubic coefficient in pitch
ρ	=	density of air
ζ	=	damping ratio
τ	=	time delay
ω	=	uncoupled natural frequency

1. Introduction

Due to various nonlinearities, aeroelastic systems exhibit a variety of phenomena such as limit cycle oscillation and chaotic vibration [1-3]. Flutter instability can jeopardize aircraft structure and its performance. A great deal of research activity devoted to flutter control of aeroelastic system has been accomplished. Kurdila et al. [4] gave an extensive review of nonlinear control methods for high-energy limit-cycle oscillations. Mukhopadhyay [5] presented an historical perspective on analysis and control of aeroelastic responses. In recent years, a large number of control strategies have been developed for the flutter suppression [6-14, 16, 17], such as adaptive decoupled fuzzy sliding-mode control [6], and tensor-product model-based control [7]. In Ref. 7, parameter-varying state-space model was transformed into the tensor-product model whereupon linear matrix inequality techniques in the parallel distributed compensation design framework can be executed to define controller. As an extension of Ref. 7, an observer was derived via LMI-based design to estimate the practically unmeasurable state values from the output values [8]. A multiple-input and multiple-output adaptive control law was designed via both leading and trailing edge control surfaces [9]. For the two-degree-of-freedom aeroelastic system with uncertainties, many effective adaptive control laws were designed by Singh et al. [10-14]. Mracek et al. [15] carried out a control design of the nonlinear benchmark problem using the state-dependent Riccati equation (SDRE) method. Then SDRE control technique was developed to design suboptimal control laws for nonlinear aeroelastic systems [16-17].

Time delays in control loops are inevitable because of the dynamics involved in the actuators, sensors, and controllers [18], and are prevalent when digital controllers, analogue anti-aliasing and reconstruction filters, and hydraulic actuators were used [19]. Time delay feedback control has received much attention recent years [20]. Chaotic motions of a two-dimensional airfoil are controlled by the application of the time-delayed continuous feedback method of Pyragas in Ref. [21]. Four control strategies are implemented with plunging displacement, plunging velocity and pitching angle, pitching velocity. It showed that the

feedback control signal derived from the pitching variables was more effective in controlling the chaotic motion of the airfoil. Time delay effects on linear/nonlinear feedback control of simple aeroelastic system were presented by Marzocca et al. [22]. In Yu et al. [23], the problem of implications of time delay feedback control of a two-dimensional supersonic lifting surface on flutter boundary is addressed. And they pointed out that we should apply both linear and nonlinear controls with small time delay, and avoid using plunging displacement controls. Zhao [18] presented a systematic study on aeroelastic stability of a two-dimensional airfoil with a single or multiple time delays in the feed back control loops. On the other side, time delay between the control input and actuators is unavoidable, and should be taken into account in the process of the control of aeroelastic system. As indicated in Ref. [22], the actuators may input energy at the moment when the controlled system does not need it. These delays can be very detrimental in the sense of impairing the control performance and can even cause irregular motions, producing instability. So it is of interest to investigate the effect of time delay on an aeroelastic system.

A state-space linear model with control input of a typical three degrees-of-freedom airfoil section was developed by Edwards et al. [24]. Conner et al. [25] successfully adapted the model to investigate the effect of structural freeplay on an open-loop system response in numerical and experimental approach. In previous research, the flutter control was studied without considering nonlinearity such as freeplay in the control surface [6-17]. In the current paper, freeplay nonlinearity in the control surface has been considered in the design of a state feedback control law for flutter suppression. With the control law designed, the effect of control surface freeplay on the dynamic response and flutter suppression have been investigated. In addition, the effect of time delay between the actuator control input and the control surface action is also investigated.

The rest of this paper is organized as follows: Section 2 presents the aeroelastic equation and control problem. A feedback control law is designed in Section 3. Section 4 shows simulation results and discussion. Conclusions are presented in Section 5.

2. Equations of Motion and Control Problem

A typical airfoil section with a trailing edge control surface is normally simplified and modelled as a three degrees-of-freedom system as illustrated in Fig. 1 for aeroelastic analysis [25]. The three degrees of freedom of the model include plunge h , pitch α , and control surface angle β . The elastic axis is located at a distance ab from the mid-chord. The airfoil mass center is located at a distance $x_\alpha b$ from the elastic axis, where b is

the semi-chord of the airfoil section. Both distances are positive when measured towards the airfoil trailing edge. There is a distance cb from the hinge line of the control surface, and a distance $x_\beta b$ from the mass center of the control surface to the mid-chord.

The non-dimensional governing equations of motion for the airfoil aeroelastic model are given by

$$\begin{aligned} r_\alpha^2 \ddot{\alpha} + [r_\beta^2 + (c-a)x_\beta] \ddot{\beta} + x_\alpha \ddot{h} + r_\alpha^2 \omega_\alpha^2 F(\alpha) &= M_\alpha / (mb^2) \\ [r_\beta^2 + (c-a)x_\beta] \ddot{\alpha} + r_\beta^2 \ddot{\beta} + x_\beta \ddot{h} + r_\beta^2 \omega_\beta^2 G(\beta) &= M_\beta / (mb^2) \\ x_\alpha \ddot{\alpha} + x_\beta \ddot{\beta} + (m_t / m) \ddot{h} + \omega_h^2 h &= L / (mb) \end{aligned} \quad (1)$$

The parameters in Eq. (1) are defined in the nomenclature. In order to keep the system response in limited cycle beyond flutter speed, a cubic nonlinear spring in pitch is considered for $F(\alpha)$ to be

$$F(\alpha) = \alpha + \gamma \alpha^3 \quad (2)$$

The control surface moment rotation relationship considering freeplay nonlinearity in the control surface is illustrated in Fig. 2 and expressed as

$$G(\beta) = \begin{cases} \beta - \delta & \beta > \delta \\ 0 & -\delta \leq \beta \leq \delta \\ \beta + \delta & \beta < -\delta \end{cases} \quad (3)$$

A structure damping matrix is created in this model according to Ref. [25, 26]. The eigenvalue λ_i , the natural frequency $\omega_i = \sqrt{\lambda_i}$, and eigenvector matrix $\mathbf{\Lambda}$ are determined from the left-hand side structure components of Eq. (1). Then the system modal mass matrix $\mathbf{M}_{mod} = \mathbf{\Lambda}^T \mathbf{M}_s \mathbf{\Lambda}$ and the modal damping matrix \mathbf{B}_{mod} can be obtained

$$\mathbf{B}_{mod} = \begin{bmatrix} 2m_\alpha \omega_\alpha \zeta_\alpha & 0 & 0 \\ 0 & 2m_\beta \omega_\beta \zeta_\beta & 0 \\ 0 & 0 & 2m_h \omega_h \zeta_h \end{bmatrix} \quad (4)$$

where m_i are the values at the diagonal entries of \mathbf{M}_{mod} , and ζ_i are the measured damping ratios. From the matrix \mathbf{B}_{mod} , the structure damping matrix can be obtained as $\mathbf{B}_s = (\mathbf{\Lambda}^T)^{-1} \mathbf{B}_{mod} (\mathbf{\Lambda})^{-1}$.

The unsteady aerodynamic force and moments in incompressible flow are given by [27]

$$\begin{aligned}
M_\alpha = & -\rho b^2 \{ \pi (1/2 - a) Ub \dot{\alpha} + \pi b^2 (1/8 + a^2) \ddot{\alpha} + (T_4 + T_{10}) U^2 \beta \\
& + [T_1 - T_8 - (c - a) T_4 + (1/2) T_{11}] Ub \dot{\beta} - [T_7 + (c - a) T_1] b^2 \ddot{\beta} - a \pi b \dot{h} \} \\
& + 2 \rho U b^2 \pi (a + 1/2) C(k) [U \alpha + \dot{h} + b(1/2 - a) \dot{\alpha} + 1/\pi T_{10} U \beta + b(1/2\pi) T_{11} \dot{\beta}]
\end{aligned} \tag{5}$$

$$\begin{aligned}
M_\beta = & -\rho b^2 \{ [-2T_9 - T_1 + T_4(a - 1/2)] Ub \dot{\alpha} + 2T_{13} b^2 \ddot{\alpha} \\
& + (1/\pi) U^2 \beta (T_5 - T_4 T_{10}) - (1/2\pi) Ub \dot{\beta} T_4 T_{11} - (1/\pi) T_3 b^2 \ddot{\beta} - T_1 b \dot{h} \} \\
& \rho U b^2 T_{12} C(k) [U \alpha + \dot{h} + b(1/2 - a) \dot{\alpha} + 1/\pi T_{10} U \beta + b(1/2\pi) T_{11} \dot{\beta}]
\end{aligned} \tag{6}$$

$$\begin{aligned}
L = & -\rho b^2 (U \pi \dot{\alpha} + \pi \dot{h} - \pi b a \ddot{\alpha} - U T_4 \dot{\beta} - T_1 b \ddot{\beta}) \\
& - 2 \pi \rho U b C(k) [U \alpha + \dot{h} + b(1/2 - a) \dot{\alpha} + 1/\pi T_{10} U \beta + b(1/2\pi) T_{11} \dot{\beta}]
\end{aligned} \tag{7}$$

The Theodorsen constants T_i , $i=1, 2, \dots, 13$, are given in Appendix A. The aerodynamic force and moments in Eq. (5) to Eq. (7) are dependent on reduced frequency k . So Eq. (1) is restricted to simple harmonic oscillation.

Aerodynamics in Eq. (5) to Eq. (7) is dependent on Theodorsen's function, $C(k)$, where k is the nondimensional reduced frequency of harmonic oscillation. So the aerodynamics is restricted to simple harmonic motion. In order to simulate arbitrary motion of the airfoil, the loading associated with Theodorsen's function $C(k)f(t)$ is replaced by the Duhamel formulation in the time domain

$$L_c = C(k) f(t) = f(0) \phi(\tau) + \int_0^\tau \frac{\partial f(\sigma)}{\partial \sigma} \phi(\tau - \sigma) d\sigma \tag{8}$$

where,

$$f(t) = U \alpha + \dot{h} + b(1/2 - a) \dot{\alpha} + 1/\pi T_{10} U \beta + b(1/2\pi) T_{11} \dot{\beta} \tag{9}$$

and $\phi(\tau)$ is Wagner function. In this paper, convenient approximation of Sears is used as

$$\phi(\tau) \approx c_0 - c_1 e^{-c_2 \tau} - c_3 e^{-c_4 \tau} \tag{10}$$

The coefficients in Eq. (10) are $c_1 = 0.165$, $c_2 = 0.0455$, $c_3 = 0.335$, and $c_4 = 0.3$.

In order to simplify the Theodorsen function, rewrite the Duhamel integral using integration by parts,

$$L_c = f(\tau) \phi(0) + \int_0^\tau f(\sigma) \frac{\partial \phi(\tau - \sigma)}{\partial \sigma} d\sigma \tag{11}$$

If we follow the state space method used by Lee et al. [28-29], six augmented states will be needed. Here, the Padé approximant method is used to represent the integral term as a second order ordinary differential equation as follow,

$$L_c = (c_0 - c_1 - c_3)f(t) + c_2c_4(c_1 + c_3)\bar{x} + (c_1c_2 + c_3c_4)\dot{\bar{x}} \quad (12)$$

After two augmented variables are introduced: $x_{a1} = \bar{x}$, $x_{a2} = \dot{\bar{x}}$, Eq. (1) can be expressed in a matrix form [30],

$$(\mathbf{M}_s - \mathbf{M}_{\text{NC}})\ddot{\mathbf{x}} + (\mathbf{B}_s - \mathbf{B}_{\text{NC}} - 1/2\mathbf{RS}_2)\dot{\mathbf{x}} + (\mathbf{K}_s - \mathbf{K}_{\text{NC}} - 1/2\mathbf{RS}_1)\mathbf{x} - \mathbf{RS}_3\mathbf{x}_a = 0 \quad (13)$$

where $\mathbf{x} = [\alpha \quad \beta \quad h/b]^T$, and $\mathbf{x}_a = [x_{a1} \quad x_{a2}]^T$. Further details of the matrices and the additional vector terms are given in Appendix B.

After introducing a variable vector $\mathbf{X} = [\mathbf{x}^T \quad \dot{\mathbf{x}}^T \quad \mathbf{x}_a^T]^T$, $\mathbf{X} \in \mathbf{R}^8$, Eq. (13) can be rewritten in a state-space form

$$\dot{\mathbf{X}} = \mathbf{A}(\mathbf{X})\mathbf{X} + \mathbf{B}\beta_c \quad (14)$$

where β_c is the command input. The definition of matrix $\mathbf{A}(\mathbf{X})$ is given in Appendix C. Matrix \mathbf{B} is given by

$$\mathbf{B} = \begin{bmatrix} 0_{3 \times 1} \\ \mathbf{M}_t^{-1}\mathbf{G} \\ 0_{2 \times 1} \end{bmatrix} \quad (15)$$

where $\mathbf{G} = \begin{bmatrix} 0 & r_\beta^2 \omega_\beta^2 & 0 \end{bmatrix}$.

If a time delay τ exists between the control input and actuator, Eq. (14) becomes

$$\dot{\mathbf{X}} = \mathbf{A}(\mathbf{X})\mathbf{X} + \mathbf{B}\beta_c(t-\tau) \quad (16)$$

3. Control Law Design and Numerical Integration

In this section, a nonlinear flutter control law based on the state-dependent Riccati equation method [15-17] is designed. Consider the optimal infinite-horizon regulator problem, the performance index J is to be minimized subject to the system expressed by Eq. (14).

$$J = \frac{1}{2} \int_0^\infty (\mathbf{X}^T \mathbf{Q}(\mathbf{X}) \mathbf{X} + r\beta_c^2) dt \quad (17)$$

where $\mathbf{Q}(\mathbf{X})$ is a positive definite symmetric matrix and $r > 0$ for $\mathbf{X} \in \mathbf{R}^8$.

For the system modeled in Eq. (14), the controllability matrix is given by

$$[\mathbf{B}, \mathbf{A}(\mathbf{X})\mathbf{B}, \mathbf{A}^2(\mathbf{X})\mathbf{B}, \dots, \mathbf{A}^8(\mathbf{X})\mathbf{B}] \quad (18)$$

In order to obtain the suboptimal solution of the preceding problem, we solve the state-dependent Riccati equation given by

$$\mathbf{A}^T(\mathbf{X})\mathbf{P}(\mathbf{X}) + \mathbf{P}(\mathbf{X})\mathbf{A}(\mathbf{X}) - \mathbf{P}(\mathbf{X})\mathbf{B}\mathbf{R}^{-1}\mathbf{B}^T\mathbf{P}(\mathbf{X}) + \mathbf{Q}(\mathbf{X}) = 0 \quad (19)$$

for a symmetric positive definite matrix $\mathbf{P}(\mathbf{X})$, the nonlinear feedback control law is given by

$$\beta_c(\mathbf{X}) = -\mathbf{R}^{-1}\mathbf{B}^T\mathbf{P}(\mathbf{X})\mathbf{X} \quad (20)$$

Substituting Eq. (20) into Eq. (14), the closed-loop system is obtained as follow

$$\dot{\mathbf{X}} = \bar{\mathbf{A}}(\mathbf{X})\mathbf{X} \quad (21)$$

where the closed-loop system matrix is given by

$$\bar{\mathbf{A}}(\mathbf{X}) = \mathbf{A}(\mathbf{X}) - \mathbf{B}\mathbf{R}^{-1}\mathbf{B}^T\mathbf{P}(\mathbf{X}) \quad (22)$$

Due to the freeplay nonlinearity in control surface, the system is divided into three distinct subdomains. In the numerical integration process, a key problem is to locate the switching point at which the system moves from one subdomain into the next. Numerical instability may occur unless the switching points are located accurately. Based on the work done by Henon [31] and Conner et al. [32], the Henon's method is developed to solve the aeroelastic control problem.

Equation (21) is then rewritten in the following form

$$\frac{d}{dt} \begin{Bmatrix} x_1 \\ x_2 \\ \vdots \\ x_8 \end{Bmatrix} = [\bar{\mathbf{A}}(\mathbf{X})] \begin{Bmatrix} x_1 \\ x_2 \\ \vdots \\ x_8 \end{Bmatrix} = \begin{Bmatrix} f_1(\mathbf{X}) \\ f_2(\mathbf{X}) \\ \vdots \\ f_8(\mathbf{X}) \end{Bmatrix} \quad (23)$$

Divide each of the state equations in Eq. (23) by $dx_2/dt = f_2(\mathbf{X})$, and replace the second equation by

$dt/dx_2 = 1/f_2(\mathbf{X})$. Then the closed-loop equation of motion can be rearranged as

$$\frac{d}{dx_2} \begin{Bmatrix} x_1 \\ t \\ \vdots \\ x_8 \end{Bmatrix} = \begin{Bmatrix} f_1(\mathbf{X})/f_2(\mathbf{X}) \\ 1/f_2(\mathbf{X}) \\ \vdots \\ f_8(\mathbf{X})/f_2(\mathbf{X}) \end{Bmatrix} \quad (24)$$

where the control surface displacement becomes an independent variable, and the time becomes a dependent variable.

By using the Runge-Kutta method, Eq. (23) is integrated forward in time until a change in the subdomain is detected. Then, the altered system (24) can be integrated using the distance from the current

control surface position to the boundary that has been crossed as step size. The result of Henon integration can be used as the initial condition to integrate the original state equation in a new subdomain until the next boundary is crossed.

4. Results and Discussion

Numerical simulation results are presented in this section. A small time step of 0.0001s is set in the process of numerical integration. The values for the system parameters are taken from Ref. [25] and listed as follows: $a = -0.5$, $b = 0.127\text{m}$, $c = 0.5$, $s = 0.52\text{m}$, $m_T = 1.2895\text{ kg}$, $I_\alpha = 0.01347\text{ kg.m}^2$, $I_\beta = 0.0003264\text{ kg.m}^2$, $x_\alpha = 0.434$, $x_\beta = 0.01996$, $k_h = 2818.8\text{ N/m}$, $S_\alpha = 0.08587\text{ kg.m}$, $S_\beta = 0.00395\text{ kg.m}$, $\rho = 1.225\text{ kg/m}^3$, $\varsigma_1 = 0.01626$, $\varsigma_2 = 0.0115$, $\varsigma_3 = 0.0113$. The nonlinear parameter in pitch stiffness is $\gamma = 3$.

4.1 Open-loop system response with freeplay nonlinearity

Starting from the open-loop stability study of the aeroelastic system, the system response keeps stable until the velocity reaches $U = 23.96\text{ m/s}$ when no freeplay exists. However, the system with freeplay exhibits limit cycle oscillation at about $U = 6.0\text{ m/s}$, which is relative to the initial conditions used in the simulation. To study the effect of control surface freeplay nonlinearity on the open-loop system response, the two values of freeplay $\delta = 1.0^\circ$ and $\delta = 2.0^\circ$ were chosen in this case to compare with the $\delta = 0^\circ$ non-freeplay system.

Flow velocity below the non-freeplay system flutter speed With the flow velocity $U = 5.0\text{ m/s}$, both freeplay and non-freeplay systems are stable. From Fig. 3, it can be observed that the freeplay system response needs more time to converge. In addition, the response amplitude is obviously bigger than the non-freeplay system. At flow velocity $U = 10.0\text{ m/s}$, the freeplay system response become limit cycle oscillation while the non-freeplay system remains stable as shown in Fig. 4. The control surface response amplitude is slightly larger than the freeplay magnitude. However the freeplay magnitude has little influence on the critical flutter velocity of the system. The system pitch and plunge amplitudes with $\delta = 2.0^\circ$ are twice larger than the amplitudes with $\delta = 1.0^\circ$.

Flow velocity above the non-freeplay system flutter speed At the flow velocity $U = 25.0\text{ m/s}$, Fig. 5 shows that the aeroelastic response of non-freeplay system becomes limit cycle oscillation. The response of freeplay system is also under limited amplitude, but not divergent, although the flow velocity is beyond the non-freeplay critical flutter speed. It indicates that the cubic nonlinearity in pitch may transform the freeplay system response from divergent motion to a limit cycle oscillation with limited amplitude. The freeplay

system responses in pitch and plunge are similar to harmonic motions with slightly larger amplitudes than the non-freeplay system responses. However, there is an obvious difference between the freeplay and non-freeplay control surface deflections as shown in Fig. 5.b. Frequency analysis of the control surface responses show that the first vibration mode component (6.0 Hz) is dominant in the non-freeplay flap response (Fig. 6.a), while the third vibration mode component (18.0 Hz) make more contribution when the freeplay exists in the control surface (Fig. 6.b). If flow velocity is continuously increased up to $U = 30.0$ m/s, the third vibration mode component (18.9 Hz) will take important role in both cases as shown in Fig. 6.c and 6.d. So the freeplay system has almost the same motion as non-freeplay system except for the phase advance as shown in Fig. 7.a.

As the existence of freeplay, the stiffness of the connection between main airfoil and control surface is reduced. When the main airfoil vibrates, the control surface is motivated through the freeplay connection. The lower connection stiffness will postpone the control surface response. But in the current case of self-excited vibration under unsteady aerodynamics, the freeplay system is easier to be excited and more sensitive to the aerodynamics. Figure 7.b shows the phase transformation process in the time history of control surface deflection. It shows the non-freeplay system response is forward in phase at the beginning until the unsteady aerodynamics become dominant in the vibration.

The analysis above indicates that the effect of freeplay on aeroelastic response is reducing as the deflection amplitude of the control surface alone with the flow velocity increases. From Fig. 2, it is noted that when the control surface deflection is small, the freeplay is dominant in the relationship between torque and the deflection. However, if the control surface deflects with larger amplitude, the linear component will become dominant. In other words, the freeplay nonlinearity has less effect and the system behaves more like a non-freeplay system as the amplitude increases.

4.2 Closed-loop system response with freeplay nonlinearity

In the following closed-loop situation, state coefficient matrix \mathbf{Q} in performance index is chose as a 8×8 unit matrix, and control input coefficient $r = 100$. To study the effect of control surface freeplay nonlinearity on the closed-loop system response, the value $\delta = 2.0^\circ$ was chosen in this case to compare with the $\delta = 0^\circ$ non-freeplay system. The simulation was first performed with the flow velocity $U = 24.0$ m/s, which is above both freeplay and non-freeplay critical flutter speed. As shown in Fig. 8, after initial oscillatory transients the plunge and pitch states converge to zero in about two seconds. There is no obvious difference between the

freeplay and non-freeplay system responses. At a higher flow velocity $U = 32.0$ m/s, a faster response time of less than one second was obtained and shown in Fig. 9. The freeplay response maximum amplitude is obviously higher. The freeplay states take more time to converge to zero after the transient oscillation, which behaves like a response of an overdamping system. Given the initial condition of $\alpha(0) = 0.1$ rad and the other variables zero, the closed-loop system will keep stable until the flow velocity reaches 84.3 m/s. While the freeplay system ($\delta = 2.0^\circ$) will show limit cycle oscillation when the flow velocity $U > 86.7$ m/s.

If the control input was triggered after the system had exhibited limit cycle oscillation, the closed-loop critical flutter speed would drop down at a lower value as a bigger control input would be required to suppress the limit cycle oscillation than the initial disturbance. For example, the critical flutter speed of the system without freeplay was reduced from 84.3 m/s to 27.3 m/s. While the freeplay ($\delta = 2.0^\circ$) led to a slight increase of the flutter speed to 27.6 m/s. This is because the freeplay makes the control surface hinge stiffness decrease. So the control surface is easier to be actuated to follow the control input. A comparison of the closed-loop responses at $U = 27.4$ m/s are shown in Fig. 10, where the controller is triggered at time $t = 2$ s after the system exhibited limit cycle oscillation. It shows that the closed-loop response without freeplay is in limit cycle oscillation with reduced amplitude, while the response with freeplay actually converges.

4.3 Closed-loop system response with time delay

In this section, the freeplay nonlinearity is ignored. Thus the standard 4-order Runge-Kutta algorithm, instead of the Henon's method is used in the integrating process. The cubic nonlinearity in pitch is preserved to prevent the system response from divergence. In this case, the simulation was conducted at the flow velocity below and above the critical flutter speed.

System response below the flutter speed First a comparison was made between the open- and closed-loop system responses at $U = 10.0$ m/s without any time delay. From the results shown in Fig. 11, it can be observed that the control law designed in section 3 makes the plunge of the closed-loop system converge much faster than the open-loop system. There is no obvious difference in the pitch response. If a time delay τ between the control input and actuator occurred at time t , the control input $\beta_c(t-\tau)$ would be derived from the previous state $\mathbf{X}(t-\tau)$ at time τ before the present state. The control input $\beta_c(t-\tau)$ would drive the system based on the state $\mathbf{X}(t-\tau)$ including deflection $\beta(t-\tau)$, which would cause oscillations of the system state and control input. It can be observed that this vibration was convergent in the beginning. When $\tau > 0.3$ ms, a high-frequency vibration of small amplitude arose in the control input $\beta_c(t)$, but the vibration is convergent.

Until $\tau \geq 1.1\text{ms}$, the vibration becomes divergent. Here, the control input was limited to a range of deflection angle $\pm 20^\circ$. The control input time histories of the close-loop system for three typical time delay sizes were shown in Fig. 12. From the analysis results, it was also found that the time delay will produce an additional motion in the system responses. Given $\tau = 2.0\text{ms}$ as an example as shown in Fig. 13, a high-frequency vibration with little amplitude occurred in company with the main vibration.

System response above the flutter speed When the flow velocity was above the system flutter speed, a control law was designed to keep the system response convergent. If a time delay was set between the control input and actuator however, the system response behaved differently. For example, the closed-loop critical flutter speed decreased from $U = 84.3\text{ m/s}$ to 47.0 m/s when a time delay of $\tau = 2.0\text{ ms}$ was set in the system. The system responses at $U = 60.0\text{ m/s}$ in terms of pitch angle and plunge displacement are shown in Fig. 14. It is obvious that the pitch and plunge responses with the time delay does not converge.

If the time delay was further increased, the designed control law would completely invalid. The system exhibit limit cycle oscillations even the flow velocity is much lower than open-loop critical flutter speed (23.96 m/s). For example, with the time delay $\tau = 10.0\text{ms}$, two typical vibration styles are performed for $U = 10.0\text{ m/s}$ and $U = 25.0\text{ m/s}$. At the flow velocity $U = 10.0\text{ m/s}$ below the open-loop critical flutter speed, the time history and phase diagram results of the system are shown in Fig. 15. The phase diagrams and Poincare section indicate that the motion is quasi-periodic. At the flow velocity $U = 25.0\text{ m/s}$ above the open-loop critical flutter speed, the phase diagrams of pitch and plunge responses are shown in Fig. 16. The system response becomes more complex than common quasi-periodic motion. But in fact, the Poincare sections in circles indicate that the motion remains as quasi-periodic motion. The study results indicate that the time delay between the control input and actuator may jeopardize the performance of a carefully designed control law, and cause instability of the system.

Keep the flow speed $U = 25.0\text{ m/s}$, bifurcation diagrams of closed-loop system response as function of time delay are given in Fig. 17. From Fig. 17.a, we can see that the system shows limit cycle oscillation after a supercritical Hopf bifurcation at about $\tau = 1.2\text{ ms}$. However, the amplitudes of pitch and plunge responses are quite small until the time delay is higher than 4.0 ms . Which means that a quite small time delay may lead to system instability, but the control law designed is still effective to depress the flutter. With the time delay increasing, closed-loop response amplitudes become large rapidly. At $\tau = 10\text{ ms}$, the pitch and plunge amplitudes are almost the same with open-loop response amplitudes. And now the control law has not any effectiveness for flutter control.

5. Conclusions

Based on the state space model of a three degrees-of-freedom airfoil section with freeplay nonlinearity, a suboptimal control law was designed by using the state-dependent Riccati equation method and applied for dynamic response suppression in this paper. In the model, a cubic nonlinearity term was adopted to prevent the aeroelastic response from divergence when the flow velocity is beyond the system critical flutter speed. The effects of both control surface freeplay and time delay between the control input and actuator on the aeroelastic responses have been investigated. The Henon's method was employed to locate the switching points in the procedure of Runge-Kutta numerical integration.

Because the linear component in the control surface response amplitude increases and becomes dominant, the effect of freeplay on the system response reduces as the flow velocity increases. In addition, the freeplay shows some beneficial effect on the aeroelastic stability of the closed-loop system. Due to the freeplay, the system response has a forward phase than the non-freeplay system response. The system response is sensitive to the time delay between the control input and actuator. The bifurcation diagram of system response as function of time delay indicates that a supercritical Hopf bifurcation occurred with a small time delay, which leads to high-frequency vibration. And with the time delay increasing, the system responses become quasi-periodic motions. It should be noted that the effect of time delay on the system response depends upon the control law designed in this paper. With alternative control laws, the system dynamic response might exhibit different phenomena. In a more realistic model, the actuator stiffness and damping should be taken into account in the controller design.

Acknowledgments

The authors would like to acknowledge the EC funding for the EU FP7 collaborative project SADE and the National Nature Science Grant of P.R. China (No. 90916006).

Appendix A: Theodorsen Constants in Eq. (5) to Eq. (7)

$$T_1 = -1/3\sqrt{1-c^2} (2+c^2) + \cos^{-1} c$$

$$T_3 = -(1/8)c(1-c^2)(5c^2+4) + 1/4(7+2c^2)\sqrt{1-c^2} \cos^{-1} c - (1/8+c^2)(\cos^{-1} c)^2$$

$$T_4 = c\sqrt{1-c^2} - \cos^{-1} c$$

$$T_5 = -(1 - c^2) + 2c\sqrt{1 - c^2} \cos^{-1} c - (\cos^{-1} c)^2$$

$$T_7 = (1/8)c(7 + 2c^2) - (1/8 + c^2)\cos^{-1} c$$

$$T_8 = -(1/3)(1 + 2c^2)\sqrt{1 - c^2} + c \cos^{-1} c$$

$$T_9 = 1/2 \left[1/3 (\sqrt{1 - c^2})^3 + aT_4 \right]$$

$$T_{10} = \sqrt{1 - c^2} + \cos^{-1} c$$

$$T_{11} = (\cos^{-1} c)(1 - 2c) + \sqrt{1 - c^2} (2 - c)$$

$$T_{12} = \sqrt{1 - c^2} (2 + c) - (\cos^{-1} c)(2c + 1)$$

$$T_{13} = 1/2 [-T_7 - (c - a)T_1]$$

Appendix B: Definitions of Matrices Appearing in Eq. (13)

$$\mathbf{M}_s = \begin{bmatrix} r_\alpha^2 & r_\beta^2 + (c - a)x_\beta & x_\alpha \\ r_\beta^2 + (c - a)x_\beta & r_\beta^2 & x_\beta \\ x_\alpha & x_\beta & M_t / M \end{bmatrix}$$

$$\mathbf{B}_s = (\mathbf{\Lambda}^T)^{-1} \begin{bmatrix} 2m_\alpha \omega_\alpha \zeta_\alpha & 0 & 0 \\ 0 & 2m_\beta \omega_\beta \zeta_\beta & 0 \\ 0 & 0 & 2m_h \omega_h \zeta_h \end{bmatrix} \mathbf{\Lambda}^{-1}$$

$$\mathbf{K}_s = \begin{bmatrix} r_\alpha^2 \omega_\alpha^2 F(\alpha) / \alpha & 0 & 0 \\ 0 & r_\beta^2 \omega_\beta^2 G(\beta) / \beta & 0 \\ 0 & 0 & \omega_h^2 \end{bmatrix}$$

$$\mathbf{M}_{\text{NC}} = -\frac{\rho}{m} \begin{bmatrix} \pi b^2 (1/8 + a^2) & -(T_7 + (c - a)T_1)b^2 & -\pi ab^2 \\ 2T_{13}b^2 & -T_3b^2 / \pi & -T_1b^2 \\ -\pi ab^2 & -T_1b^2 & \pi b^2 \end{bmatrix}$$

$$\mathbf{B}_{\text{NC}} = -\frac{\rho}{m} \begin{bmatrix} \pi(1/2 - a)Ub & (T_1 - T_8 - (c - a)T_4 + T_{11}/2)Ub & 0 \\ (-2T_9 - T_1 + T_4(a - 1/2))Ub & -T_4T_{11}Ub / (2\pi) & 0 \\ \pi Ub & -UT_4b & 0 \end{bmatrix}$$

$$\mathbf{K}_{\text{NC}} = -\frac{\rho}{m} \begin{bmatrix} 0 & (T_4 + T_{10})U^2 & 0 \\ 0 & (T_5 - T_4 T_{10})U^2 / \pi & 0 \\ 0 & 0 & 0 \end{bmatrix}$$

$$\mathbf{R} = [2\pi\rho U(a + 1/2)/m \quad -\rho U T_{12}/m \quad -2\pi\rho U/m]^T$$

$$\mathbf{S}_1 = [U \quad T_{10}U/\pi \quad 0]$$

$$\mathbf{S}_2 = [b(1/2 - a) \quad bT_{11}/2\pi \quad b]$$

$$\mathbf{S}_3 = [c_2 c_4 (c_1 + c_3)U^2/b \quad (c_1 c_2 + c_3 c_4)U].$$

Appendix C: Definitions of Matrices Appearing in Eq. (14)

$$\mathbf{A} = \begin{bmatrix} 0 & \mathbf{I}_{3 \times 3} & 0 \\ -\mathbf{M}_t^{-1} \mathbf{K}_t & -\mathbf{M}_t^{-1} \mathbf{B}_t & \mathbf{M}_t^{-1} \mathbf{D} \\ \mathbf{E}_1 & \mathbf{E}_2 & \mathbf{F} \end{bmatrix},$$

where, $\mathbf{M}_t = \mathbf{M}_s - \mathbf{M}_{\text{NC}}$, $\mathbf{B}_t = \mathbf{B}_s - \mathbf{B}_{\text{NC}} - 1/2 \mathbf{R} \mathbf{S}_2$, $\mathbf{K}_t = \mathbf{K}_s - \mathbf{K}_{\text{NC}} - 1/2 \mathbf{R} \mathbf{S}_1$, $\mathbf{D} = \mathbf{R} \mathbf{S}_3$,

$$\mathbf{E}_1 = \begin{bmatrix} 0 & 0 & 0 \\ U/b & U T_{10}/(\pi b) & 0 \end{bmatrix}, \quad \mathbf{E}_2 = \begin{bmatrix} 0 & 0 & 0 \\ (1/2 - a) & T_{11}/(2\pi) & 1 \end{bmatrix}, \quad \mathbf{F} = \begin{bmatrix} 0 & 1 \\ -c_2 c_4 U^2/b & -(c_2 + c_4)U/b \end{bmatrix}.$$

References

- [1] B.H.K. Lee, S.J. Price, Y.S. Wong, Nonlinear aeroelastic analysis of airfoil: bifurcation and chaos, *Progress in Aerospace Science* 35 (1999) 205-334.
- [2] E.H. Dowell, J. Edwards, T. Strganac, Nonlinear aeroelasticity, *Journal of Aircraft* 40 (2003) 857-874.
- [3] D. Li, J. Xiang, Chaotic motions of an airfoil with cubic nonlinearity in subsonic flow, *Journal of Aircraft*, 45 (2008) 1457-1460.
- [4] A.J. Kurdila, T.W. Strganac, J.L. Junkins, J. Ko, M.R. Akella, Nonlinear control methods for high-energy limit-cycle oscillations, *Journal of Guidance, Control, and Dynamics* 24 (2001) 185-192.
- [5] V. Mukhopadhyay, Historical perspective on analysis and control of aeroelastic responses, *Journal of Guidance, Control, and Dynamics* 26 (2003) 673-684.
- [6] C. M. Lin, W.L. Chin, Adaptive decoupled fuzzy sliding-model control of a nonlinear aeroelastic system, *Journal of Guidance, Control, and Dynamics* 29 (2006) 206-209.
- [7] P. Baranyi, Tensor-product model-based control of two-dimensional aeroelastic system, *Journal of Guidance, Control, and Dynamics* 29 (2006) 391-400.

- [8] P. Baranyi, Out feedback control of two-dimensional aeroelastic system, *Journal of Guidance, Control, and Dynamics* 29 (2006) 762-767.
- [9] A. Bihal, V.M. Rao, P. Marzocca, Adaptive control for a nonlinear wing section with multiple flaps, *Journal of Guidance, Control, and Dynamics* 29 (2006) 744-748.
- [10] S.N. Singh, L. Wang, Output feedback form and adaptive stabilization of a nonlinear aeroelastic system. *Journal of Guidance, Control, and Dynamics* 25(2002) 725-732.
- [11] S.N. Singh, M. Brenner, Modular adaptive control of a nonlinear aeroelastic system. *Journal of Guidance, Control, and Dynamics* 26 (2003) 443-451.
- [12] W. Xing, S.N. Singh, Adaptive output feedback control of a nonlinear aeroelastic structure. *Journal of Guidance, Control, and Dynamics* 23 (2000) 1109-1136.
- [13] R. Zhang, S.N. Singh, Adaptive output feedback control of an aeroelastic system with unstructured uncertainties. *Journal of Guidance, Control, and Dynamics* 24 (2001) 502-509.
- [14] K.W. Lee, S.N. Singh, Global robust control of an aeroelastic system using output feedback," *Journal of Guidance, Control, and Dynamics* 30 (2007) 271-275.
- [15] C.P. Mracek, J.R. Cloutier, Control designs for the nonlinear benchmark problem via the state-dependent Riccati equation method, *International Journal of Robust and Nonlinear Control* 8 (1998) 401-433.
- [16] M. Tadi, State-dependent Riccati equation for control of aeroelastic flutter, *Journal of Guidance, Control, and Dynamics* 26 (2003) 914-917.
- [17] N. Bhoir , S.N. Singh, Control of unsteady aeroelastic system via state-dependent Riccati equation method, *Journal of Guidance, Control, and Dynamics* 28 (2005) 78-84.
- [18] Y. H. Zhao, Stability of a two-dimensional airfoil with time-delayed feedback control, *Journal of Fluids and Structures* 25 (2009) 1-25.
- [19] H.Y. Hu, E.H. Dowell, L. N. Virgin, Stability estimation of high dimensional vibrating system under state delay feedback control, *Journal of Sound and Vibration* 214 (1998) 497-511.
- [20] C.Z. Qian, J.S. Tang, A time delay control for a nonlinear dynamic beam under moving load, *Journal of Sound and Vibration* 309 (2008) 1-8.
- [21] M. Ramesh, S. Narayanan, Controlling chaotic motions in a two-dimensional airfoil using time-delay feedback, *Journal of Sound and Vibration* 239 (2001) 1037-1049.
- [22] P. Marzocca, L. Librescu, W.A. Silva, Time-delay effects on linear/ nonlinear feedback control of simple aeroelastic systems, *Journal of Guidance, Control, and Dynamics* 28 (2005) 53-62.

- [23] P. Yu, Z. Chen, L. Librescu, P. Marzocca, Implications of time-delayed feedback control on limit cycle oscillation of a two-dimensional supersonic lifting surface, *Journal of Sound and Vibration* 304 (2007) 974-986.
- [24] J.W. Edwards, H. Ashley, J.V. Breakwell, Unsteady Aerodynamic Modeling for Arbitrary Motions, *AIAA Journal* 17 (1979) 365-374.
- [25] M.D. Conner, D.M. Tang, E.H. Dowell, L.N. Virgin, Nonlinear behavior of a typical airfoil section with control surface freeplay: a numerical and experimental Study, *Journal of Fluids and structures* 11 (1997) 89-109.
- [26] L. Liu, E.H. Dowell, Harmonic balance approach for an airfoil with a freeplay control surface, *AIAA Journal*, 43 (2005) 802-815.
- [27] T. Theodorsen, General theory of aerodynamic instability and the mechanism of flutter, NACA Report 496, 1935.
- [28] B.H.K. Lee, L. Gong, Y.S. Wong, Analysis and computation of nonlinear dynamic response of a two-degree-of-freedom system and its application in aeroelasticity, *Journal of Fluids and Structures* 11 (1997) 225-246.
- [29] B.H.K. Lee, L. Liu, K.W. Chung, Airfoil motion in subsonic flow with strong cubic nonlinear restoring forces, *Journal of Sound and Vibration*, 281 (2005) 699-717.
- [30] S.T. Trickey, Global and local dynamics of an aeroelastic system with a control surface freeplay nonlinearity, PhD Thesis, Duke University, 2000.
- [31] M. Henon, On the numerical computation of Poincaré map, *Physica D* 5 (1982) 412-414.
- [32] M.D. Conner, L.N. Virgin, E.H. Dowell, Accurate numerical integration of state-space models for aeroelastic systems with free play, *AIAA Journal* 34 (1996) 2202-2205.

Figure Captions

Fig. 1. Schematic of airfoil section with a control surface.

Fig. 2. Freeplay nonlinearity.

Fig. 3. Time histories of open-loop aeroelastic systems at $U = 5.0$ m/s: a) pitch; b) flap; c) plunge.

Fig. 4. Time histories of open-loop aeroelastic systems at $U = 10.0$ m/s: a) pitch; b) flap; c) plunge.

Fig. 5. Time histories of open-loop aeroelastic systems at $U = 25.0$ m/s: a) pitch; b) flap; c) plunge.

Fig. 6. Frequency analysis of flap deflection for a) and b): at $U = 25.0$ m/s; c) and d): at $U = 30.0$ m/s.

Fig. 7. Time histories of open-loop aeroelastic systems at $U = 30.0$ m/s: a) stable; b) transient.

Fig. 8. Aeroelastic flutter suppression with and without freeplay at $U = 24.0$ m/s: a) pitch; b) plunge.

Fig. 9. Aeroelastic flutter suppression with and without freeplay at $U = 32.0$ m/s: a) pitch; b) plunge.

Fig. 10. Aeroelastic flutter suppression with and without freeplay at $U = 27.4$ m/s: a) pitch; b) plunge.

Fig. 11. Open-loop and closed-loop responses at $U = 10.0$ m/s, $\tau = 0.0$ ms: a) pitch; b) plunge.

Fig. 12. Time histories of control input at $U = 10.0$ m/s and: a) $\tau = 0.5$ ms; b) $\tau = 1.0$ ms; c) $\tau = 1.1$ ms.

Fig. 13. Closed-loop responses with and without time delay at $U = 10.0$ m/s, $\tau = 2.0$ ms: a) pitch; b) plunge.

Fig. 14. Time histories at $U = 60.0$ m/s, $\tau = 2.0$ ms: a) pitch; b) plunge.

Fig. 15. Time histories a) pitch; b) plunge; phase diagrams c) pitch; d) plunge; and Poincare sections e) pitch; f) plunge at $U = 10.0$ m/s, $\tau = 10.0$ ms.

Fig. 16. Time histories a) pitch; b) plunge; phase diagrams c) pitch; d) plunge; and Poincare sections e) pitch; f) plunge at $U = 25.0$ m/s, $\tau = 10.0$ ms.

Fig. 17. Bifurcation diagrams of a) pitch; b) plunge response as function of time delay at $U = 25.0$ m/s.

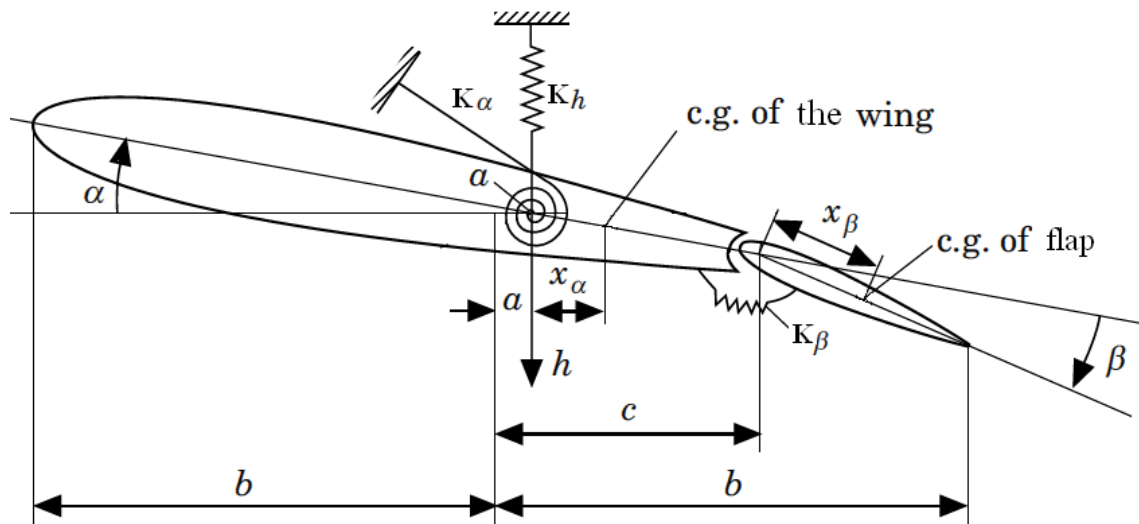


Fig. 1. Schematic of airfoil section with a control surface.

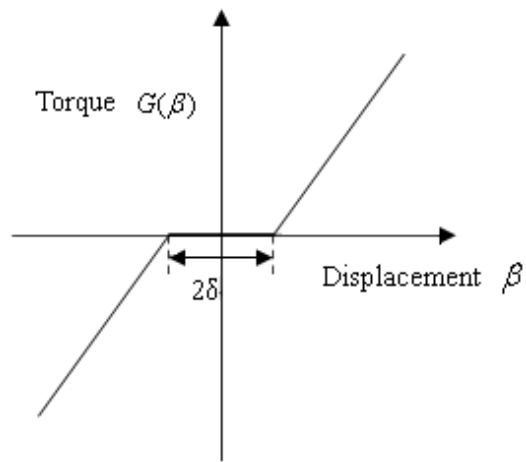


Fig. 2. Freeplay nonlinearity.

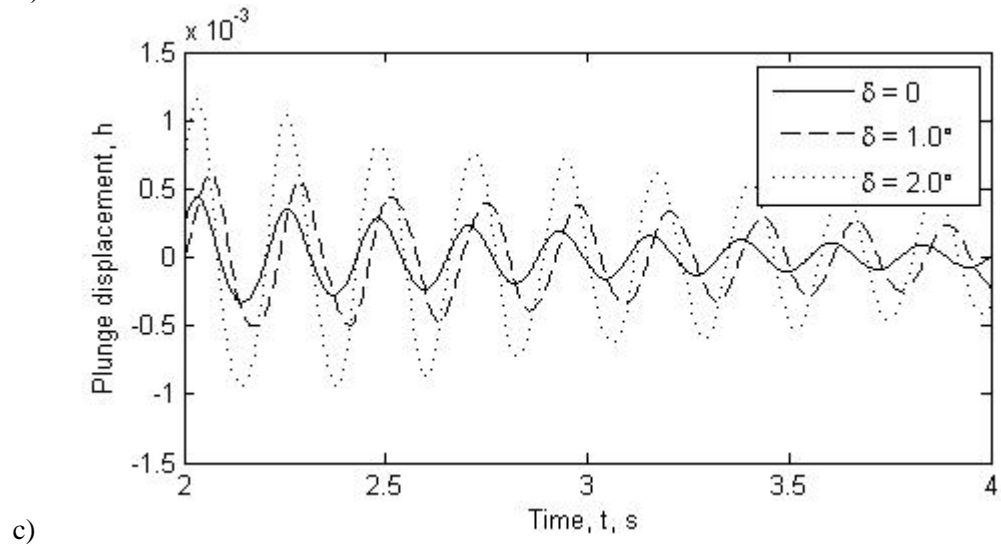
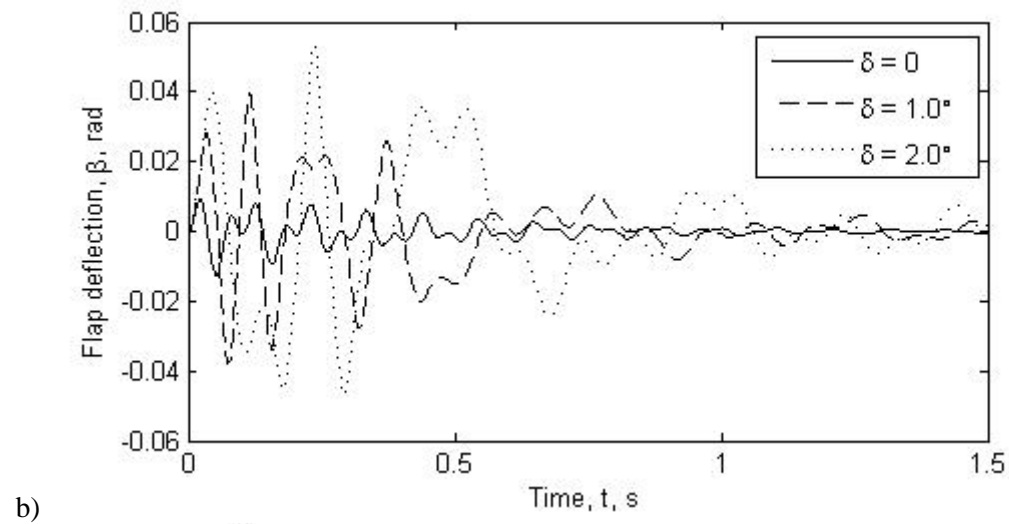
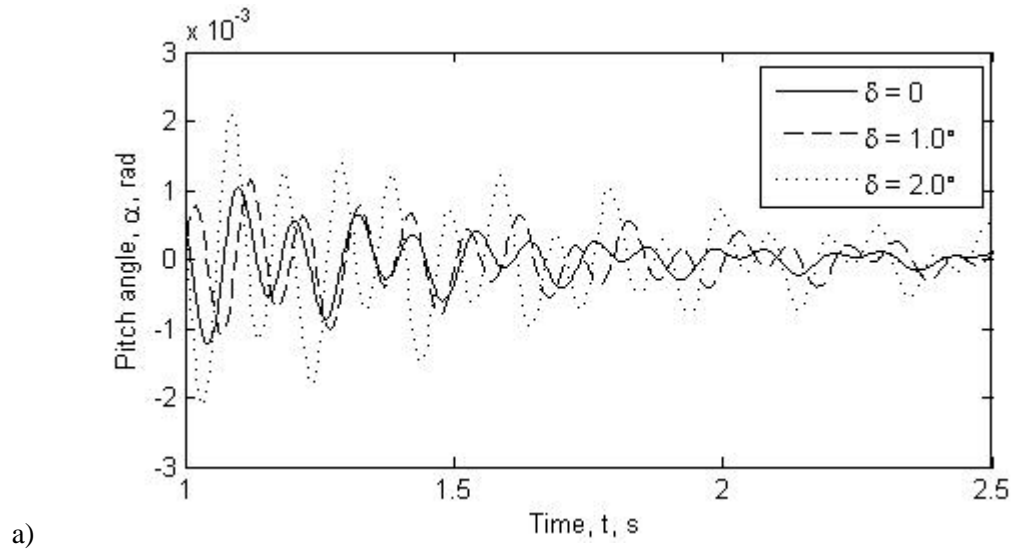


Fig. 3. Time histories of open-loop aeroelastic systems at $U = 5.0$ m/s: a) pitch; b) flap; c) plunge.

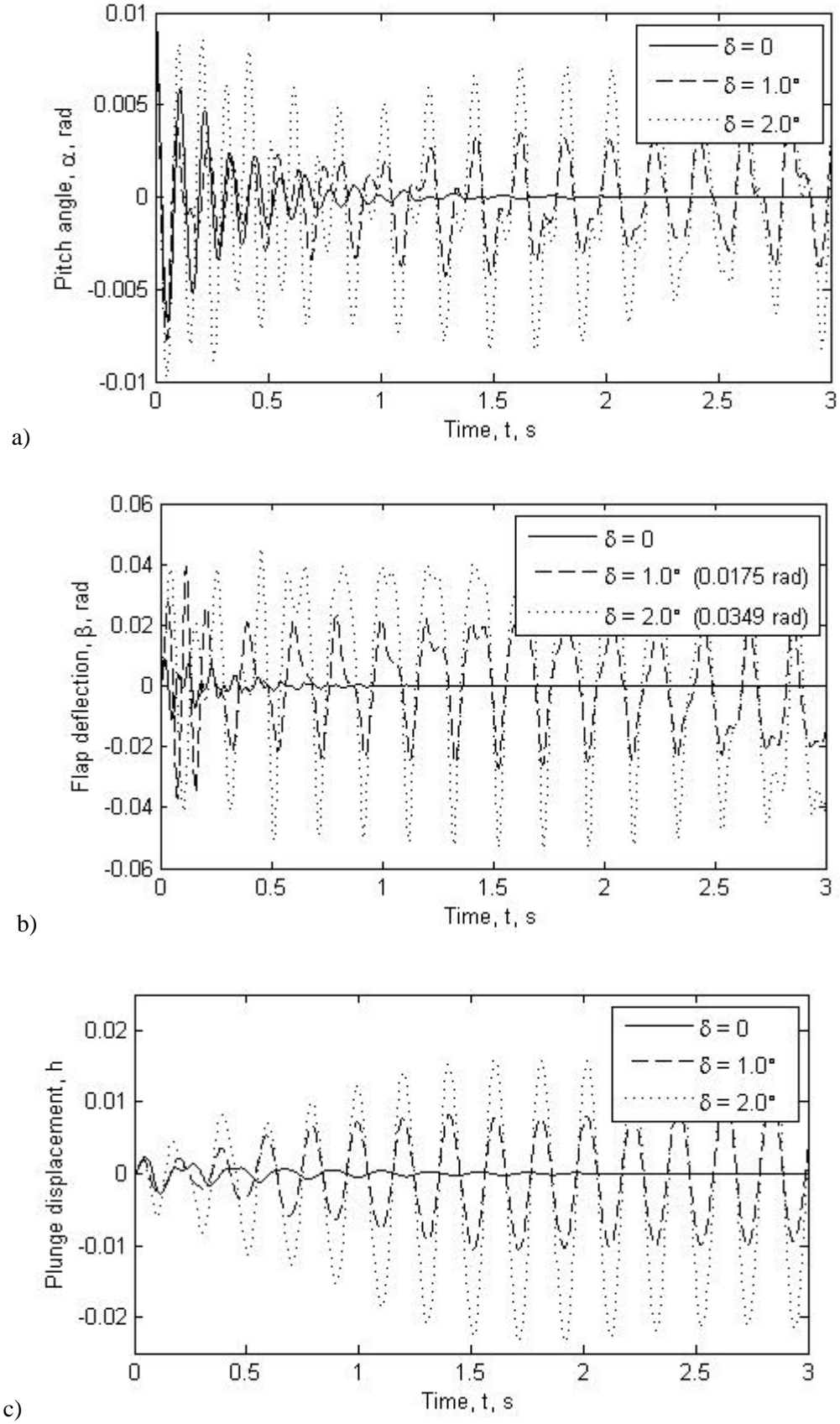


Fig. 4. Time histories of open-loop aeroelastic systems at $U = 10.0$ m/s: a) pitch; b) flap; c) plunge.

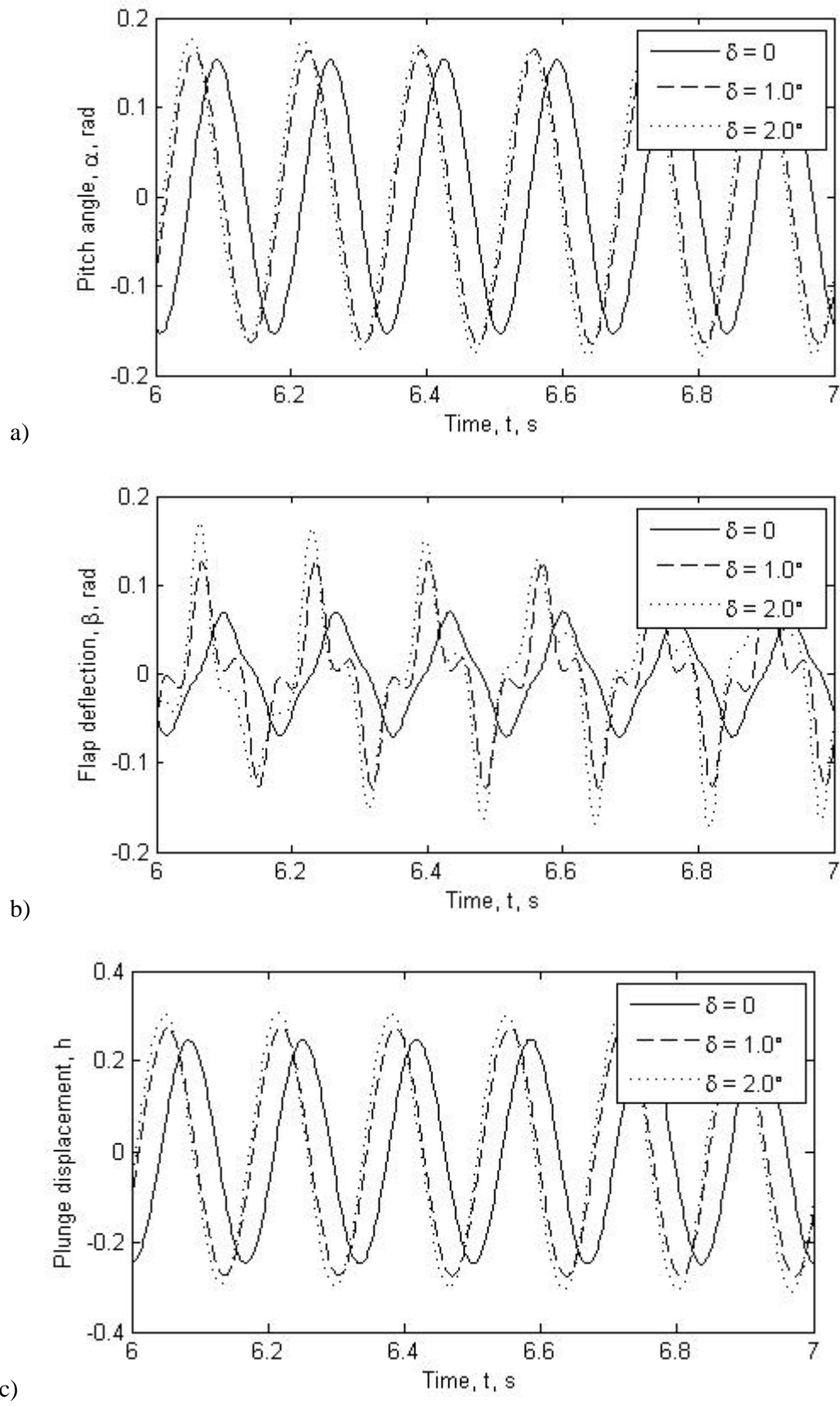


Fig. 5. Time histories of open-loop aeroelastic systems at $U = 25.0$ m/s: a) pitch; b) flap; c) plunge.

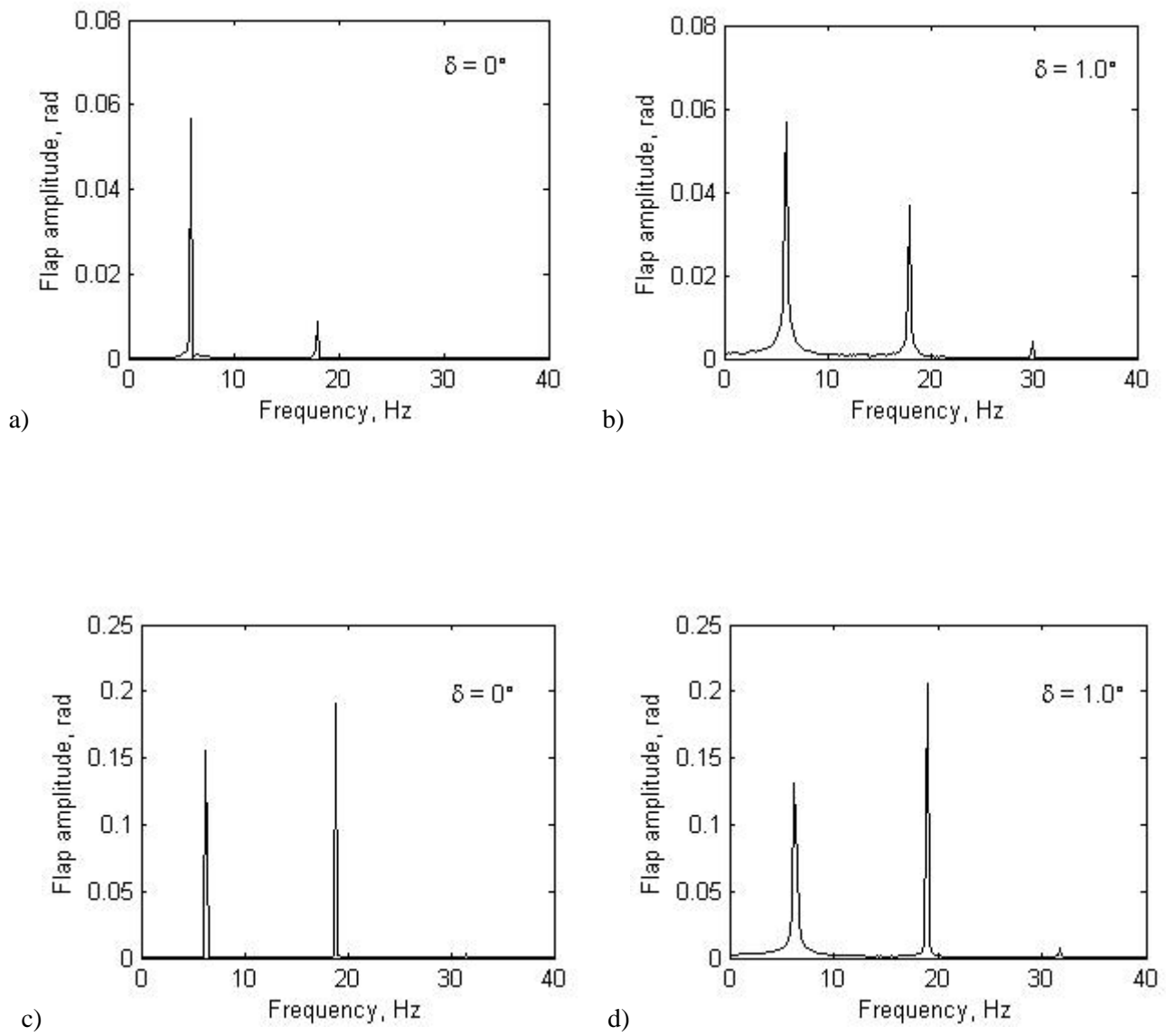


Fig. 6. Frequency analysis of flap deflection for a) and b): at $U = 25.0$ m/s; c) and d): at $U = 30.0$ m/s.

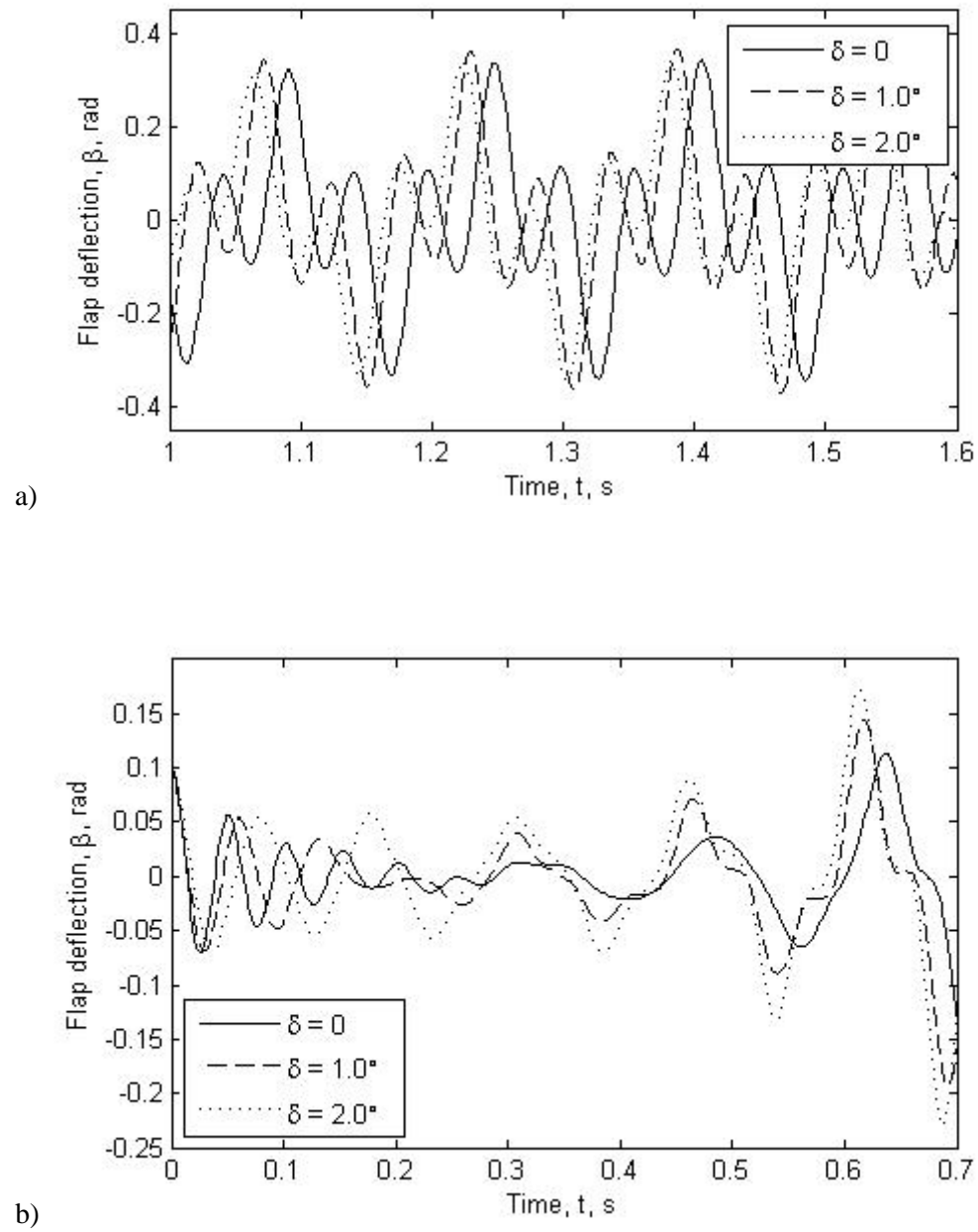
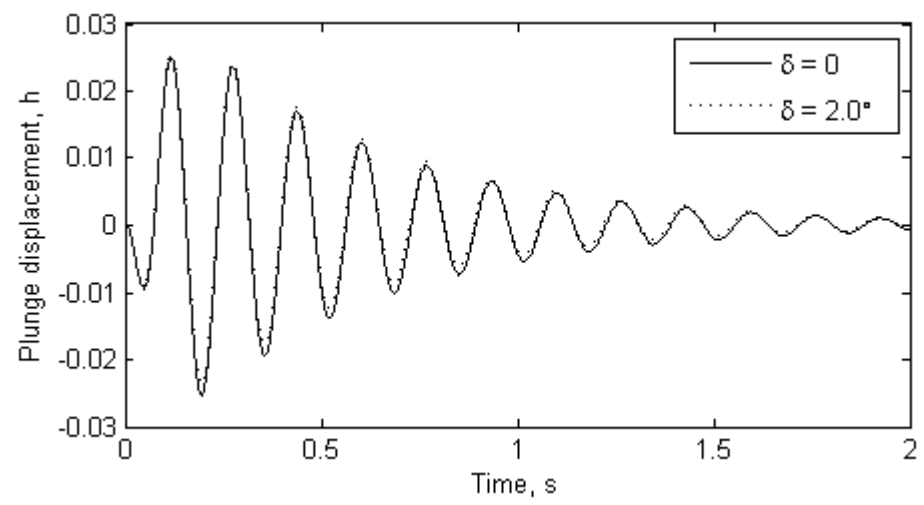
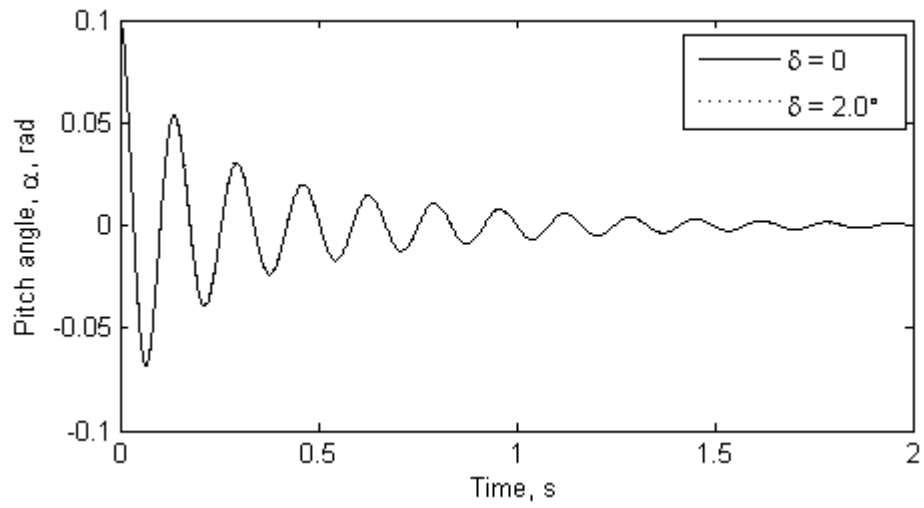


Fig. 7. Time histories of open-loop aeroelastic systems at $U = 30.0$ m/s: a) stable; b) transient.



b)

Fig. 8. Aeroelastic flutter suppression with and without freeplay at $U = 24.0$ m/s: a) pitch; b) plunge.

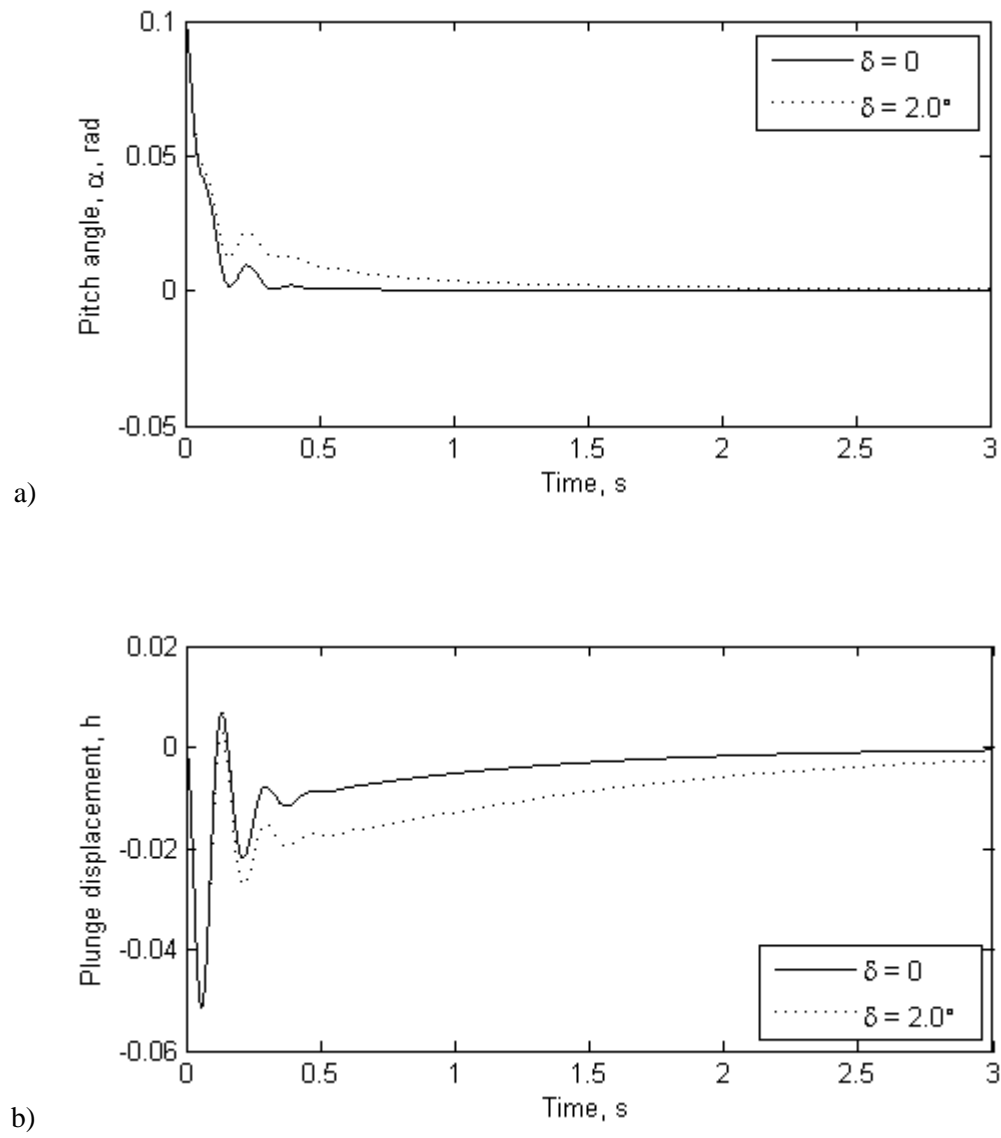


Fig. 9. Aeroelastic flutter suppression with and without freeplay at $U = 32.0$ m/s: a) pitch; b) plunge.

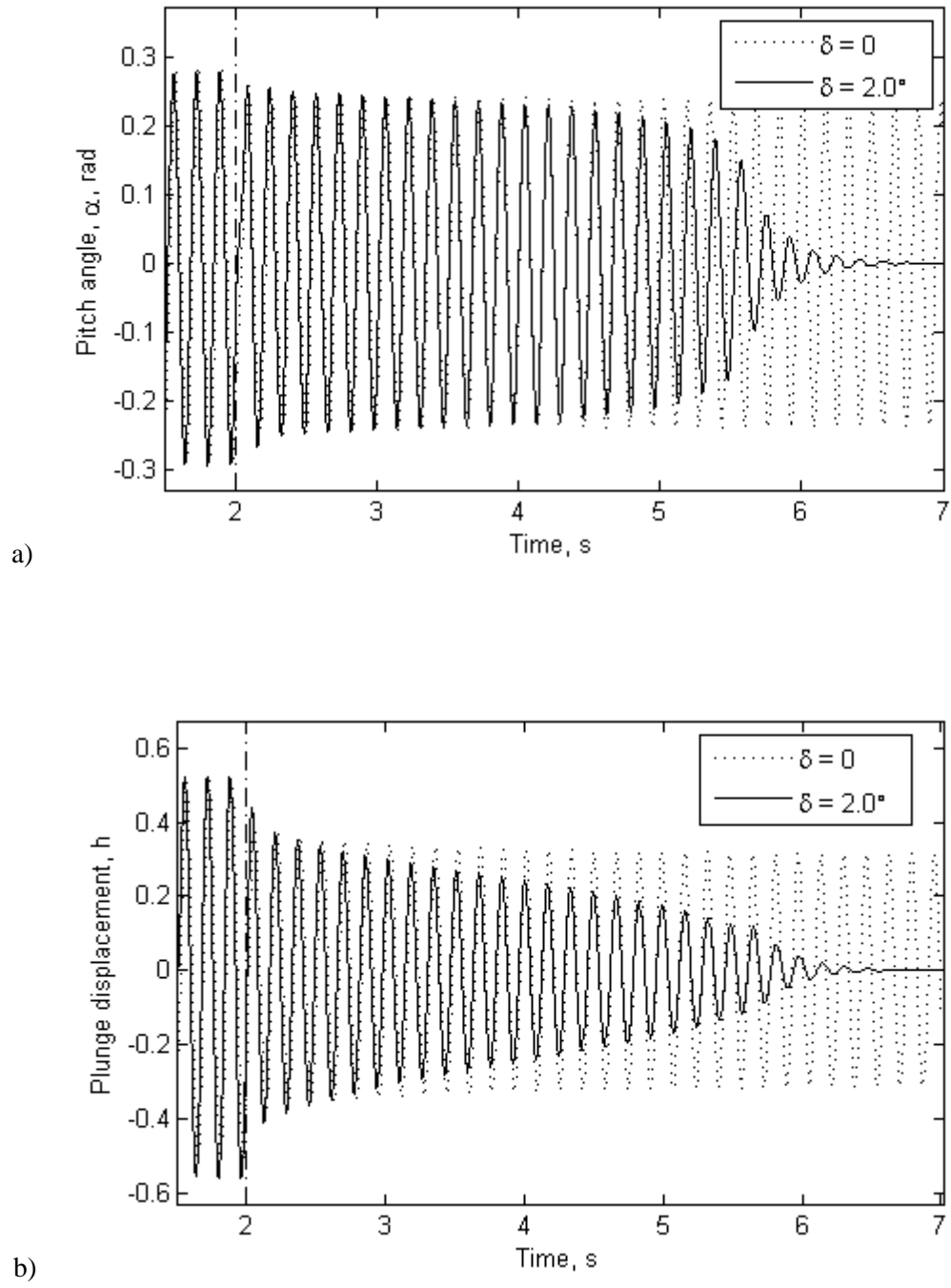


Fig. 10. Aeroelastic flutter suppression with and without freeplay at $U = 27.4$ m/s: a) pitch; b) plunge.

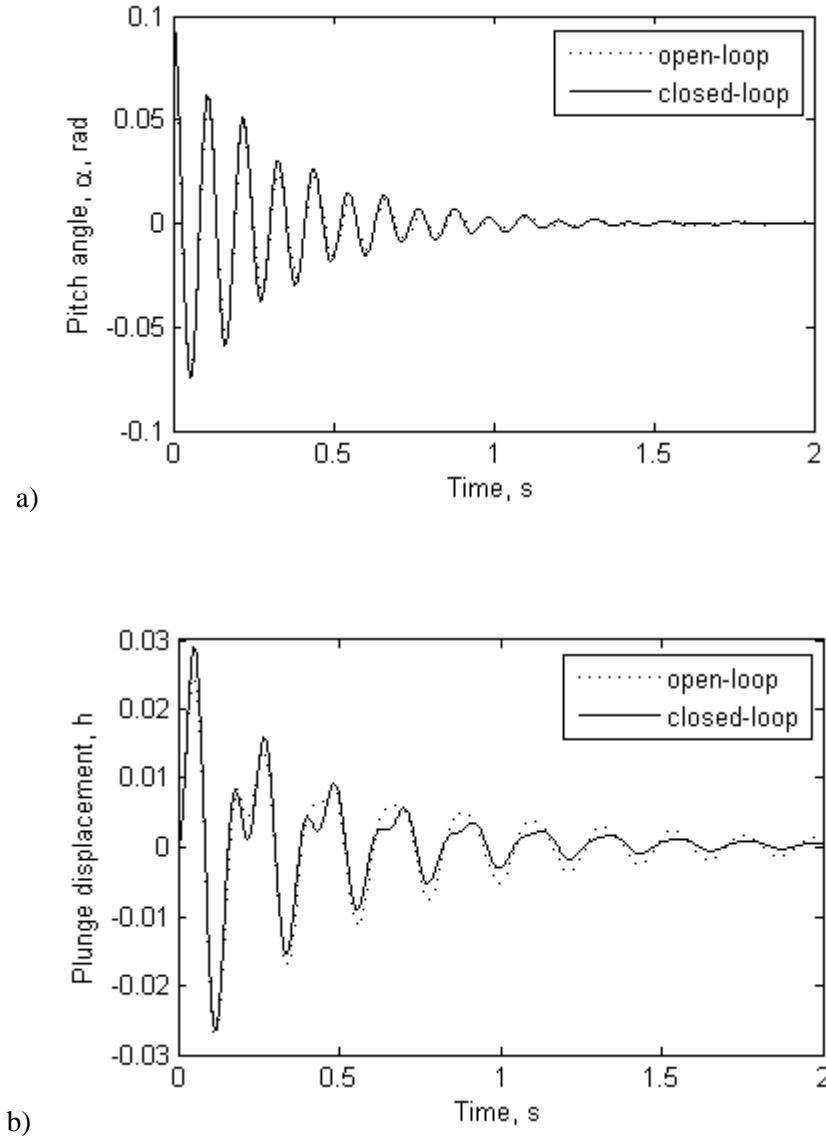


Fig. 11. Open-loop and closed-loop responses at $U = 10.0$ m/s, $\tau = 0.0$ ms: a) pitch; b) plunge.

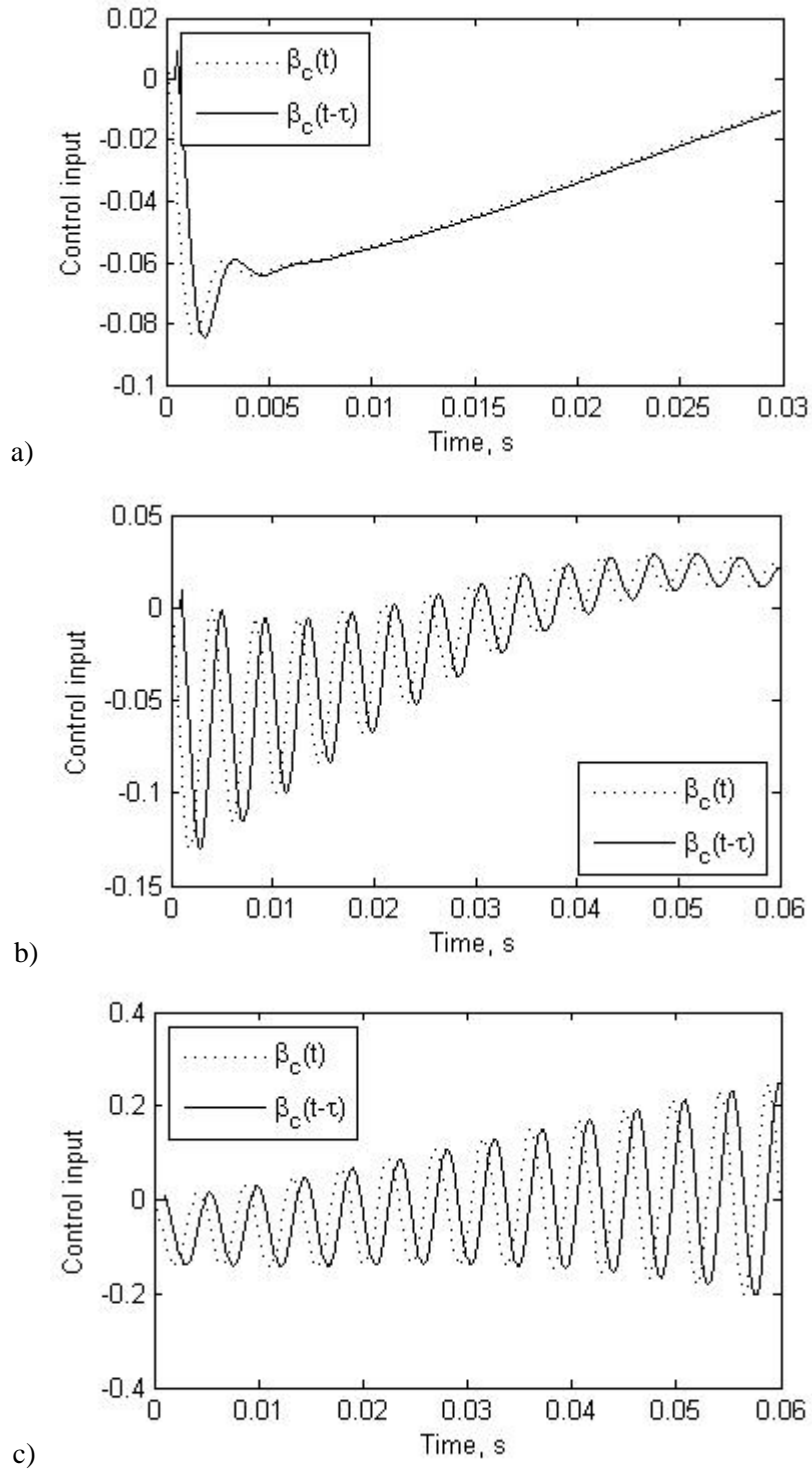


Fig. 12. Time histories of control input at $U = 10.0$ m/s and: a) $\tau = 0.5$ ms; b) $\tau = 1.0$ ms; c) $\tau = 1.1$ ms.

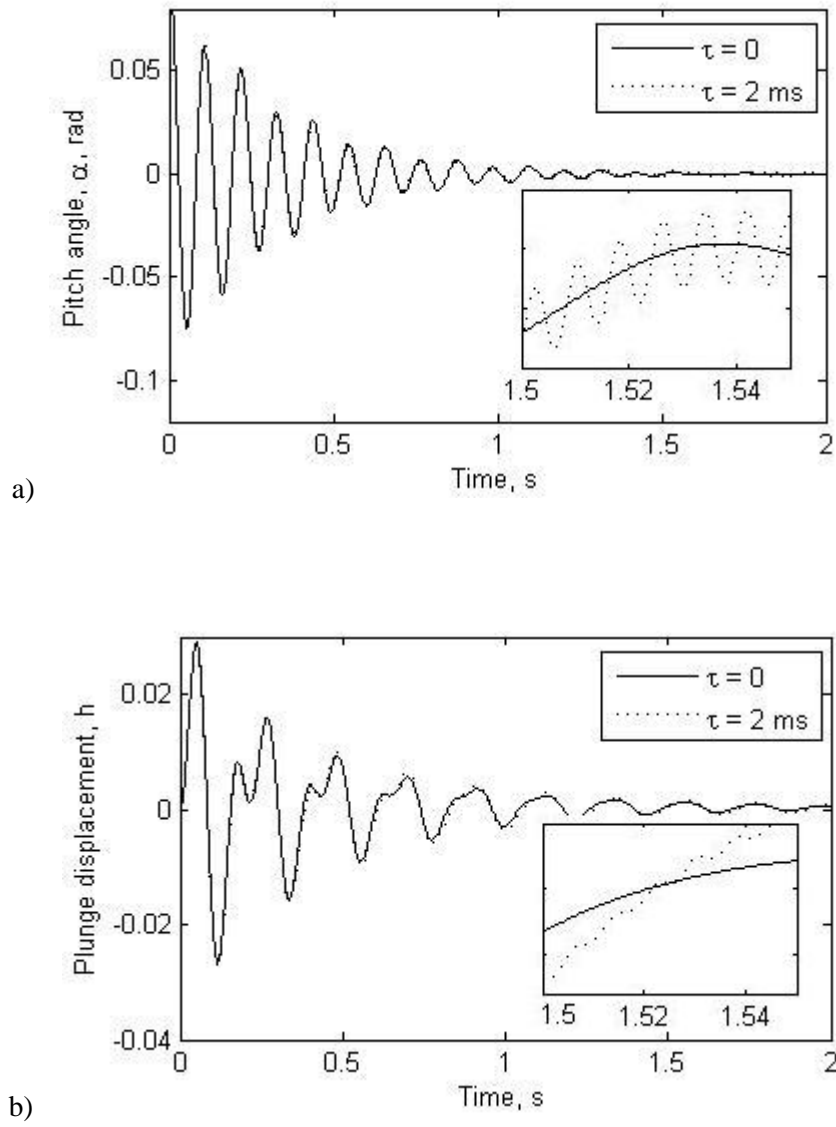


Fig. 13. Closed-loop responses with and without time delay at $U = 10.0$ m/s, $\tau = 2.0$ ms: a) pitch; b) plunge.

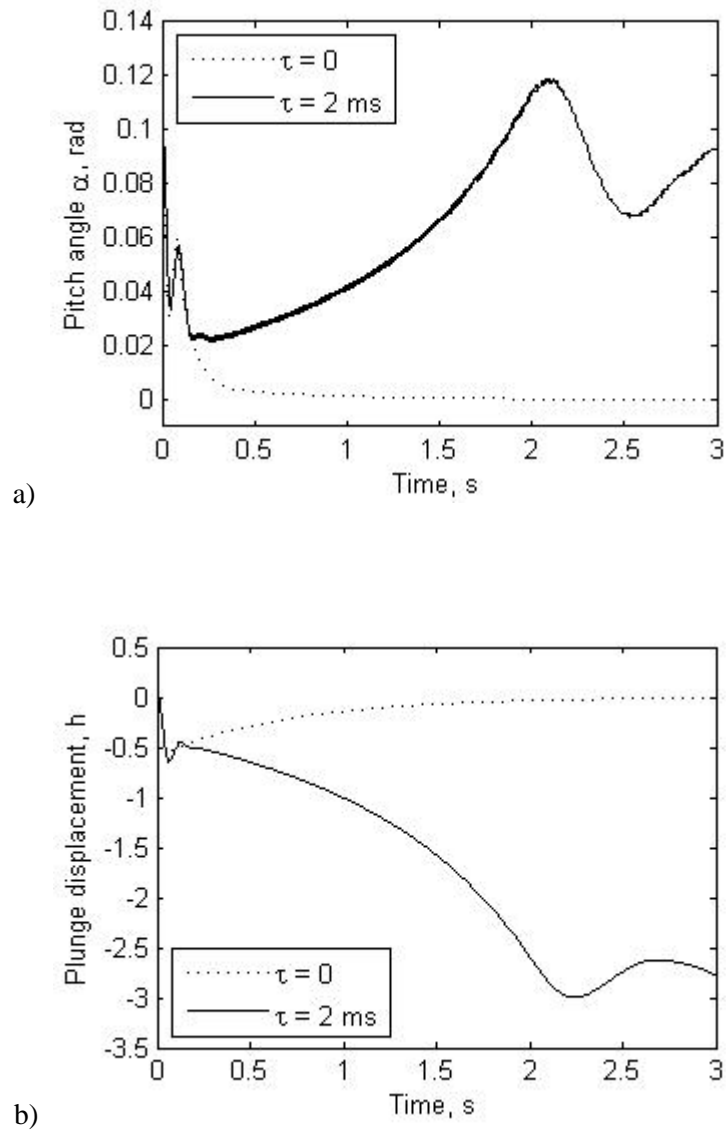


Fig. 14. Time histories at $U = 60.0$ m/s, $\tau = 2.0$ ms: a) pitch; b) plunge.

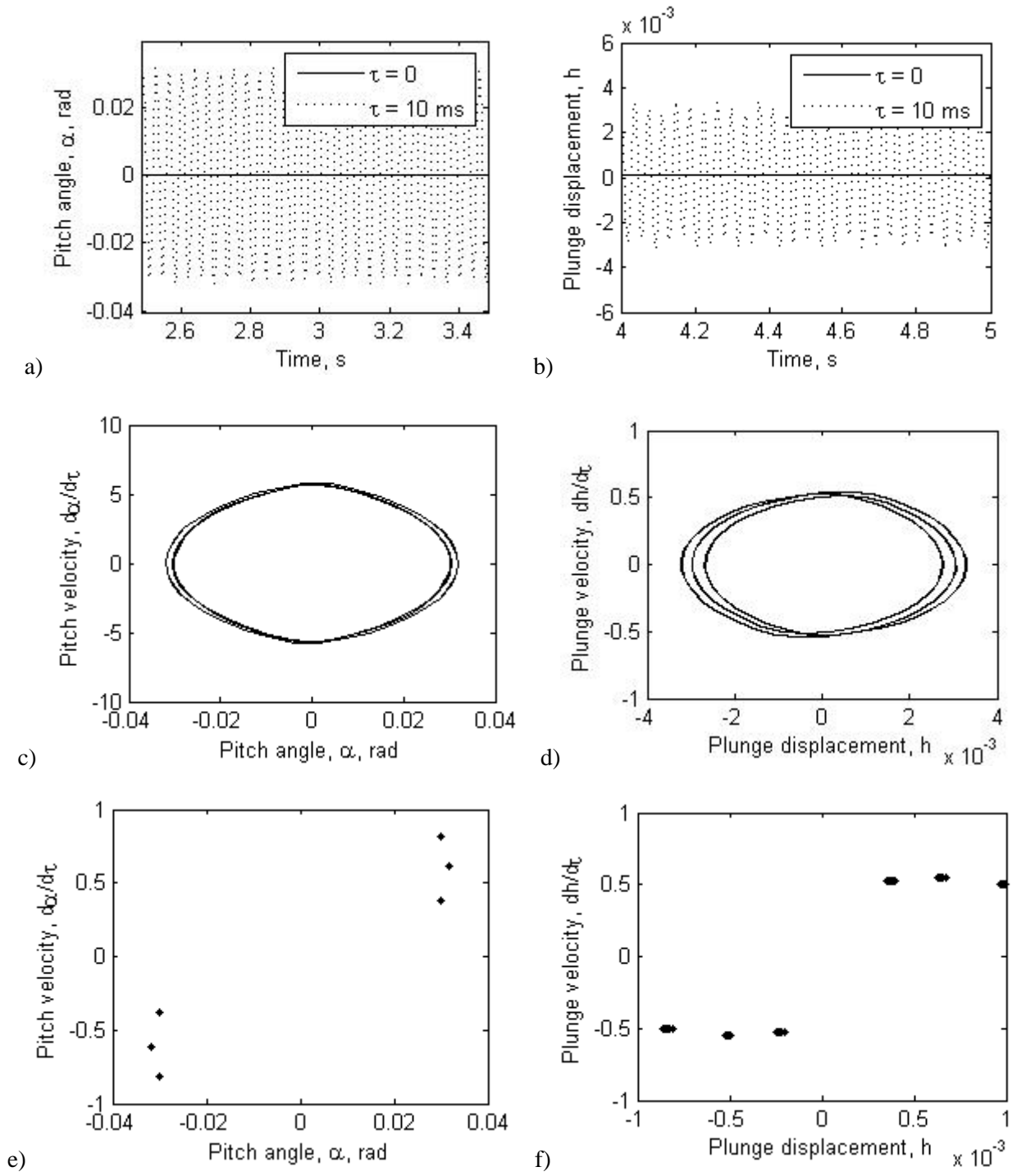


Fig. 15. Time histories a) pitch; b) plunge; phase diagrams c) pitch; d) and plunge Poincaré sections e) pitch; f) plunge at $U = 10.0$ m/s, $\tau = 10.0$ ms.

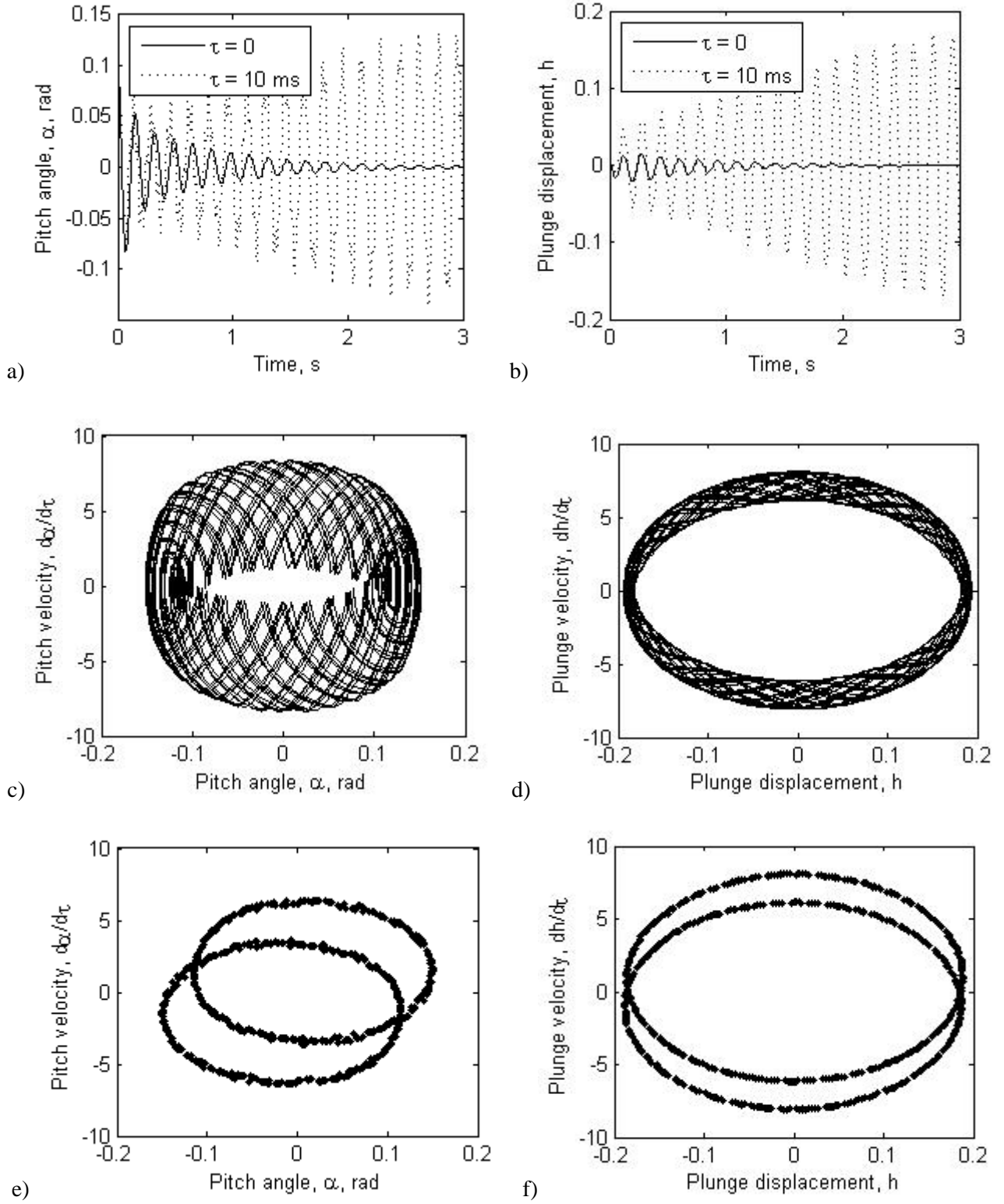


Fig. 16. Time histories a) pitch; b) plunge; phase diagrams c) pitch; d) plunge; and Poincare sections e) pitch; f) plunge at $U = 25.0$ m/s, $\tau = 10.0$ ms.

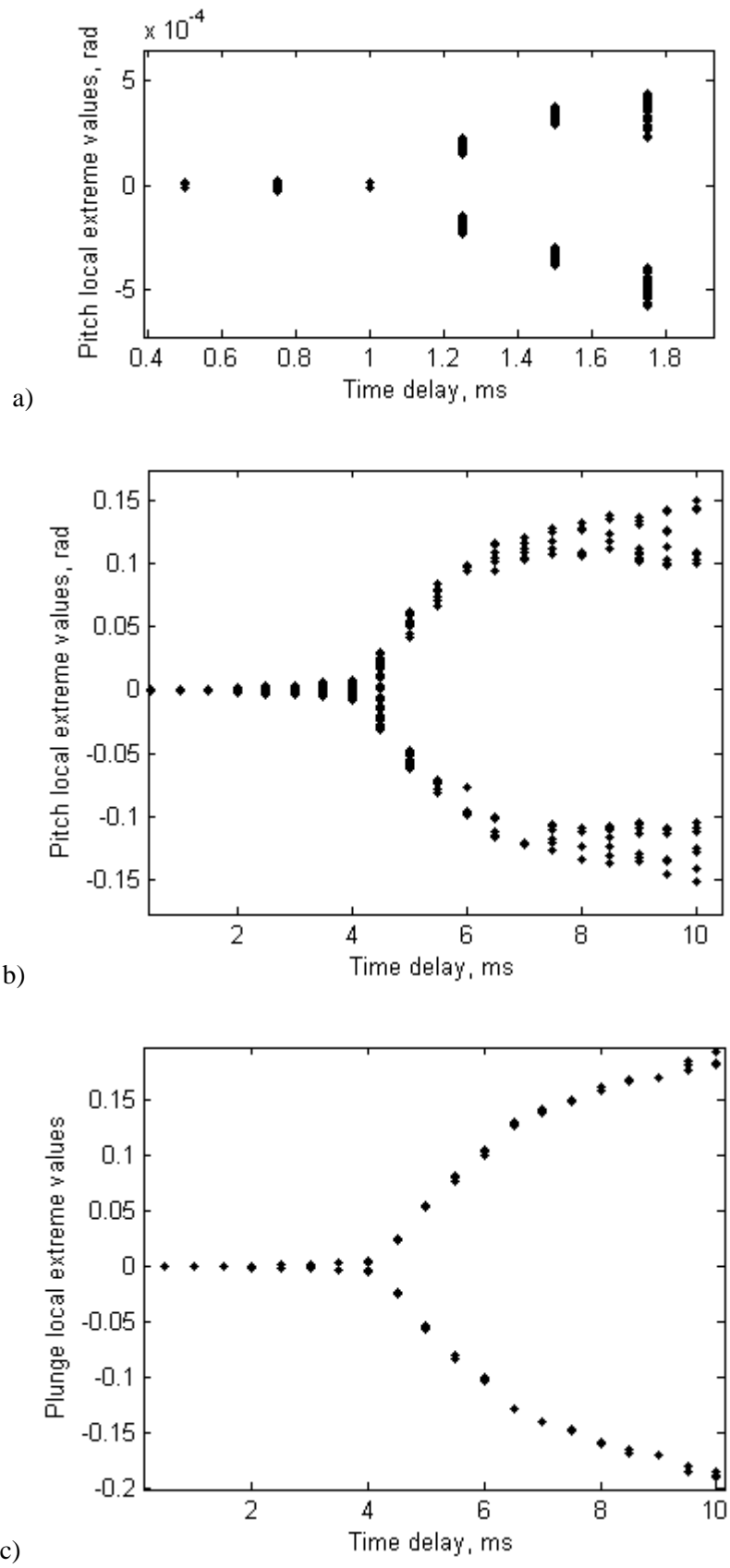


Fig. 17. Bifurcation diagrams of a) , b) pitch and c) plunge response as function of time delay at $U = 25.0$

m/s.

Aeroelastic dynamic response and control of an airfoil section with control surface nonlinearities

Li, Daochun

2010-10-25

Daochun Li, Shijun Guo, Jinwu Xiang. (2010) Aeroelastic dynamic response and control of an airfoil section with control surface nonlinearities. Journal of Sound and Vibration, Volume 329, Issue 22, October 2010, pp 4756-4771

<https://doi.org/10.1016/j.jsv.2010.06.006>

Downloaded from CERES Research Repository, Cranfield University